Quantum cascade lasers with integrated plasmonic antenna-array collimators

Nanfang Yu[1], Romain Blanchard[1], Jonathan Fan[1], Qi Jie Wang[1], Christian Pflügl[1], Laurent Diehl[1], Tadataka Edamura[2], Masamichi Yamanishi[2], Hirofumi Kan[2], and Federico Capasso[1,*]

[1]*School of Engineering and Applied Sciences, Harvard University, Cambridge, Massachusetts 02138, U.S.A.*
[2]*Central Research Laboratory, Hamamatsu Photonics K.K., Hamamatsu 434-8601, Japan*
**Corresponding author: capasso@seas.harvard.edu*

Abstract: We demonstrated in simulations and experiments that by defining a properly designed two-dimensional metallic aperture-grating structure on the facet of quantum cascade lasers, a small beam divergence angle can be achieved in directions both perpendicular and parallel to the laser waveguide layers (denoted as $\theta_{\perp}$ and $\theta_{\parallel}$, respectively). Beam divergence angles as small as $\theta_{\perp}=2.7^{o}$ and $\theta_{\parallel}=3.7^{o}$ have been demonstrated. This is a reduction by a factor of ~30 and ~10, respectively, compared to those of the original lasers emitting at a wavelength of 8.06 μm. The devices preserve good room temperature performance with output power as high as ~55% of that of the original unpatterned lasers. We studied in detail the trade-off between beam divergence and power throughput for the fabricated devices. We demonstrated plasmonic collimation for buried heterostructure lasers and ridge lasers; devices with different waveguide structures but with the same plasmonic collimator design showed similar performance. We also studied a device patterned with a "spider's web" pattern, which gives us insight into the distribution of surface plasmons on the laser facet.

OCIS codes: (120.1680) Collimation; (140.5965) Semiconductor lasers, quantum cascade; (240.6680) Surface plasmons

References and Links

1. H. A. Atwater, "The promise of plasmonics," Sci. Am. **296**, 56-63 (2007).
2. E. Ozbay, "Plasmonics: merging photonics and electronics at nanoscale dimensions," Science **311**, 189-193 (2006).
3. E. Cubukcu, E. A. Kort, K. B. Crozier, and F. Capasso, "Plasmonic laser antenna," Appl. Phys. Lett. **89**, 093120 (2006).
4. N. Yu, E. Cubukcu, L. Diehl, M. A. Belkin, K. B. Crozier, F. Capasso, D. Bour, S. Corzine, and G. Höfler, "Plasmonic quantum cascade laser antenna," Appl. Phys. Lett. **91**, 173113 (2007).
5. N. Yu, E. Cubukcu, L. Diehl, D. Bour, S. Corzine, J. Zhu, G. Höfler, K. B. Crozier, and F. Capasso, "Bowtie plasmonic quantum cascade laser antenna," Opt. Express **15**, 13272-13281 (2007).
6. T. Mukaihara, N. Ohnoki, Y. Hayashi, N. Hatori, F. Koyama, and K. Iga, "Polarization control of vertical-cavity surface-emitting lasers using a birefringent metal/dielectric polarizer loaded on top distributed Bragg reflector," IEEE J Sel. Topics Quantum Electron. **1**, 667-673 (1995).
7. J.-H. Ser, Y.-G. Ju, J.-H. Shin, and Y. H. Lee, "Polarization stabilization of vertical-cavity top-surface-emitting lasers by inscription of fine metal-interlaced gratings," Appl. Phys. Lett. **66**, 2769-2771 (1995).
8. C.-A. Berseth, B. Dwir, I. Utke, H. Pier, A. Rudra, V. P. Iakovlev, E. Kapon, and M. Moser, "Vertical cavity surface emitting lasers incorporating structured mirrors patterned by electron-beam lithography," J. Vac. Sci. Technol. B **17**, 3222-3225 (1999).
9. P. Debernardi, J. M. Ostermann, M. Feneberg, C. Jalics, and R. Michalzik, "Reliable polarization control of VCSELs through monolithically integrated surface gratings: a comparative theoretical and experimental study," IEEE J Sel. Topics Quantum Electron. **11**, 107-116 (2005).

#100120 - $15.00 USD Received 13 Aug 2008; revised 19 Sep 2008; accepted 21 Sep 2008; published 10 Nov 2008

10. S. Boutami, B. Benbakir, J.-L. Leclercq, and P. Viktorovitch, "Compact and polarization controlled 1.55 μm vertical-cavity surface emitting laser using single-layer photonic crystal mirror," Appl. Phys. Lett. **91**, 071105 (2007).
11. P. Babu Dayal and F. Koyama, "Polarization control of 0.85 μm vertical-cavity surface-emitting lasers integrated with gold nanorod arrays," Appl. Phys. Lett. **91**, 111107 (2007).
12. M. C. Y. Huang, Y. Zhou, and C. J. Chang-Hasnain, "A surface-emitting laser incorporating a high-index-contrast subwavelength grating," Nat. Photonics **1**, 119-122 (2007).
13. H. J. Lezec, A. Degiron, E. Devaux, R. A. Linke, L. Martin-Moreno, F. J. Garcia-Vidal, and T. W. Ebbesen, "Beaming light from a subwavelength aperture," Science **297**, 820-822 (2002).
14. J. Gao, G. Song, Q. Gan, B. Guo, and L. Chen, "Surface plasmon modulated nano-aperture vertical-cavity surface-emitting laser," Laser Phys. Lett. **4**, 234-237 (2007).
15. J. Feng, T. Okamoto, and S. Kawata, "Highly directional emission via coupled surface-plasmon tunneling from electroluminescence in organic light-emitting devices," Appl. Phys. Lett. **87**, 241109 (2005).
16. J. Feng and T. Okamoto, "Enhancement of electroluminescence through a two-dimensional corrugated metal film by grating-induced surface-plasmon cross coupling," Opt. Lett. **30**, 2302-2304 (2005).
17. M. D. Harries and H. D. Summers, "Directional control of light-emitting-diode emission via a subwavelength-apertured metal surface," IEEE Photon. Tech. Lett. **18**, 2197-2199 (2006).
18. D. Hofstetter, J. Faist, M. Beck, and U. Oesterle, "Surface-emitting 10.1 μm quantum-cascade distributed feedback lasers," Appl. Phys. Lett. **75**, 3769-3771 (1999).
19. W. Schrenk, N. Finger, S. Gianordoli, L. Hvozdara, G. Strasser, and E. Gornik, "Surface-emitting distributed feedback quantum-cascade lasers, " Appl. Phys. Lett. **77**, 2086-2088 (2000).
20. C. Pflügl, M. Austerer, W. Schrenk, S. Golka, G. Strasser, R. P. Green, L. R. Wilson, J. W. Cockburn, A. B. Krysa, and J. S. Roberts, "Single-mode surface-emitting quantum-cascade lasers," Appl. Phys. Lett. **86**, 211101 (2005).
21. N. Yu, J. Fan, Q. J. Wang, C. Pflügl, L. Diehl, T. Edamura, M. Yamanishi, H. Kan, and F. Capasso, "Small-divergence semiconductor lasers by plasmonic collimation," Nat. Photonics **2**, 564-570 (2008).
22. N. Yu, R. Blanchard, J. Fan, T. Edamura, M. Yamanishi, H. Kan, and F. Capasso, "Small divergence semiconductor lasers with two-dimensional plasmonic collimators," Appl. Phys. Lett. (to appear).
23. L. Martín-Moreno, F. J. García-Vidal, H. J. Lezec, A. Degiron, and T. W. Ebbesen, "Theory of highly directional emission from a single subwavelength aperture surrounded by surface corrugations," Phys. Rev. Lett. **90**, 167401 (2003).
24. L.-B. Yu, D.-Z. Lin, Y.-C. Chen, Y.-C. Chang, K.-T. Huang, J.-W. Liaw, J.-T. Yeh, J.-M. Liu, C.-S. Yeh, and C.-K. Lee, "Physical origin of directional beaming emitted from a subwavelength slit," Phys. Rev. B **71**, 041405(R) (2005).
25. F. J. García-Vidal, L. Martín-Moreno, H. J. Lezec, and T. W. Ebbesen, "Focusing light with a single subwavelength aperture flanked by surface corrugations," Appl. Phys. Lett. **83**, 4500-4502 (2003).
26. J. A. Kong, *Electromagnetic Wave Theory* (EMW Publishing, Cambridge, 2000).
27. S. -H. Chang, S. Gray, and G. Schatz, "Surface plasmon generation and light transmission by isolated nanoholes and arrays of nanoholes in thin metal films," Opt. Express **13**, 3150-3165 (2005).
28. L. Yin, V. K. Vlasko-Vlasov, A. Rydh, J. Pearson, U. Welp, S.-H. Chang, S. K. Gray, G. C. Schatz, D. B. Brown, and C. W. Kimball, "Surface plasmons at single nanoholes in Au films," Appl. Phys. Lett. **85**, 467-469 (2004).
29. J. M. Steele, Z. Liu, Y. Wang, and X. Zhang, "Resonant and non-resonant generation and focusing of surface plasmons with circular gratings," Opt. Express **14**, 5664-5670 (2006).
30. A. Taflove, and S. C. Hagness, *Computational Electrodynamics: the Finite-Difference Time-Domain Method*, 2nd edition (Artech House Publishers, Norwood, Massachusetts, 2000).
31. W. L. Barnes, T. W. Preist, S. C. Kitson, and J. R. Sambles, "Physical origin of photonic energy gaps in the propagation of surface plasmons on gratings," Phys. Rev. B **54**, 6227 - 6244 (1996).
32. G. Lévêque, O. J. F. Martin, and J. Weiner, "Transient behavior of surface plasmon polaritons scattered at a subwavelength groove," Phys. Rev. B **76**, 155418 (2007).
33. G. Gay, O. Alloschery, B. Viaris de Lesegno, C. O'Dwyer, J. Weiner, and H. J. Lezec, "The optical response of nanostructured surfaces and the composite diffracted evanescent wave model," Nat. Phys. **2**, 262-267 (2006).
34. P. Lalanne and J. P. Hugonin, "Interaction between optical nano-objects at metallo-dielectric interfaces," Nat. Phys. **2**, 551-556 (2006).
35. L. Novotny and B. Hecht, *Principles of Nano-Optics* (Cambridge University Press, Cambridge, 2006).
36. A symmetric grating provides minimum momentum for flipping the direction of the SP wavevector.
37. K. Fujita, S. Furuta, A. Sugiyama, T. Ochiai, T. Edamura, N. Akikusa, M. Yamanishi, and H. Kan, "Room temperature, continuous-wave operation of quantum cascade lasers with single phonon resonance-continuum depopulation structures grown by metal organic vapor-phase epitaxy," Appl. Phys. Lett. **91**, 141121 (2007).
38. S. Y. Chou, P. R. Krauss, and P. J. Renstrom, "Imprint lithography with 25-nanometer resolution," Science

#100120 - $15.00 USD Received 13 Aug 2008; revised 19 Sep 2008; accepted 21 Sep 2008; published 10 Nov 2008

272, 85-87 (1996).
39. P. C. Hidber, W. Helbig, E. Kim, and G. M. Whitesides, "Microcontact printing of Palladium colloids: micron-scale patterning by electroless deposition of copper," Langmuir **12**, 1375-1380 (1996).

1. Introduction

Plasmonics enables manipulation of light at the subwavelength level [1,2]. Plasmonic structures integrated on active optical devices provide major opportunities to engineer the emission wavefront, thus enabling complex beam shaping both in the near field and in the far field.

For near-field applications, plasmonic laser antennas have been created to concentrate light into deep subwavelength regions with high optical intensity for near-infrared laser diodes and mid-infrared quantum cascade lasers (QCLs) [3-5]. For far-field applications, plasmonics has been used for beam shaping and polarization control of light sources. For instance, metallic gratings and nanorod arrays were shown to be able to efficiently select the polarization of the output of vertical-cavity surface-emitting lasers (VCSELs) [6-12]. Lezec and coworkers' demonstrated that a plasmonic aperture-groove structure defined in a suspended metallic film can collimate incident light [13]. Guo and coauthors used a similar design to reduce the beam divergence of VCSELs by about a factor of two [14]. It has also been demonstrated that highly directional emission can be produced by patterning two-dimensional (2D) periodical metallic films (metallic photonic crystals) on the large facet of light-emitting diodes (LEDs) [15-17]. Despite of these efforts, highly directional emission within a few degrees using plasmonics has not been realized for edge-emitting semiconductor lasers, which have small light-emitting regions.

Compact laser sources with highly directional output are desirable for many applications such as free space communication, remote sensing, and pointing, as these applications require light to be concentrated in a small solid angle in the far field. Collimated lasers are also important for applications such as optical communications, to couple laser output into optical fibers and waveguides. Semiconductor lasers, however, usually have a large beam divergence, due to diffraction at their small light-emitting apertures. Edge-emitting semiconductor lasers such as diode lasers and mid-infrared QCLs have particularly small apertures and their full-width at half-maximum (FWHM) divergence angles are in the range of several tens of degrees. VCSELs benefit from a larger aperture but still have a sizable divergence, ranging from 5 to 30 degrees. The problem of large beam divergence for semiconductor lasers is conventionally addressed by using lenses or curved mirrors, which are usually expensive and require meticulous alignment. Another approach is to process lasers into surface-emitting devices. Surface-emitting QCLs with second-order distributed feedback gratings have been shown to have very small beam divergence in the direction along the laser ridge [18-20].

Recently, our group has demonstrated a very small beam divergence in the laser polarization direction for λ=9.9 μm QCLs by patterning a one-dimensional (1D) plasmonic grating on the laser facet [21]. We then extended the idea to 2D plasmonic structures and achieved collimation in both the vertical and lateral directions for QCLs [22]. We report here an extensive study of mid-infrared QC lasers with 2D collimation. 2D plasmonic collimation was demonstrated for both ridge QCLs (λ=9.95 μm) and buried heterostructure (BHT) QCLs (λ=8.06 μm). It is shown that the divergence angles are greatly reduced, down to just a few degrees. The fabricated devices preserve good room temperature performances; the devices with an optimized design exhibit an output power that is above half of that of the original unpatterned lasers.

Plasmonic collimation has many benefits compared with conventional collimation techniques. Firstly, the plasmonic collimator is integrated with the laser so it requires no alignment. Secondly, by proper scaling of the plasmonic collimator design, it can fit onto any type of semiconductor laser with a wide range of emitting wavelengths from visible to THz. This is helpful especially for spectral regions where lenses are expensive. For example,

#100120 - $15.00 USD Received 13 Aug 2008; revised 19 Sep 2008; accepted 21 Sep 2008; published 10 Nov 2008

mid-infrared (mid-ir) lenses are quite expensive due to scarcity of materials that are transparent in this wavelength range. Conventionally, to efficiently collect optical power emitted from semiconductor lasers, lenses with a high numerical aperture (NA), are needed. Plasmonic collimation coupled with a low NA lens would boost the collected power and reduce the cost of the collimation system. Lastly, the plasmonic collimator is essentially able to control the beam divergence in two orthogonal directions. This is helpful for some applications where a collimated beam with circular cross section is required to reduce aberration along the optical path.

2. Design

A sketch of our design is shown in Fig. 1. It is based on experimental and theoretical works on the beaming of light displayed by an aperture-grating structure [13,23-25]. A subwavelength aperture is opened in a metal layer on the laser facet. It couples a portion of the beam emerging from the laser active core into surface plasmons (SPs). The SPs propagate along the metal coated facet and are scattered by an ensemble of periodic grooves defined on the facet. The direct emission from the aperture and the secondary beams coming from the grooves interfere constructively, so that the energy is radiated into a small solid angle in the far field. The aperture and the grooves in the plasmonic collimator act essentially as an array of coherent light sources, much in analogy to phased antenna arrays [26]. The latter have been widely used to enhance the directivity of antennas for applications such as directional broadcasting and space communications. Theoretically, the beam divergence angle of our devices with plasmonic collimators should be inversely proportional to the number of the grooves N, while the intensity of the small divergence beam should be approximately proportional to N^2.

To achieve small divergence angles, high power throughput, and small optical background outside of the collimated beam, several geometrical parameters of the plasmonic collimator need to be optimized. These parameters include the shape of the grating grooves, the aperture sizes $w_1 \times w_2$, the grating period Λ, the width w and depth d of the grooves, and the position of the grating relative to the aperture. The following paragraphs discuss physical considerations for choosing these parameters.

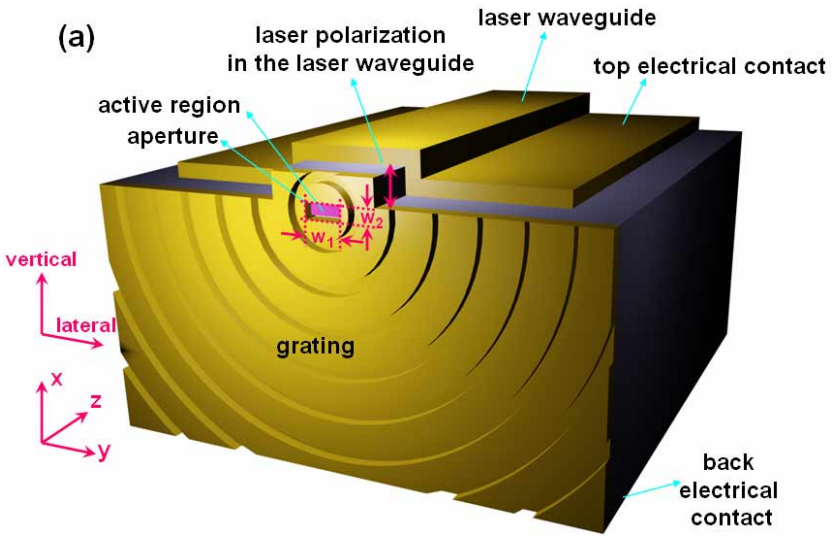

Fig. 1. A sketch of the device, consisting of a quantum cascade laser and a metallic aperture-grating structure defined on its facet.

#100120 - $15.00 USD Received 13 Aug 2008; revised 19 Sep 2008; accepted 21 Sep 2008; published 10 Nov 2008

2.1 Shape of the grating grooves

We choose a ring grating so that the shape of the grating grooves matches the SP wavefront. This is confirmed by our finite-element simulations (COMSOL Multiphysics), which indicate that the SP wavefront is approximately circular for a rectangular aperture with lateral size w_1 =2-10 μm and vertical size w_2=2 μm, where w_1 and w_2 are shown in Fig. 1.

2.2 Aperture size

For 2D collimation, efficient SP propagation in both vertical and lateral directions (x and y axes in Fig. 1) has to be achieved. Because QCLs are TM polarized with electric field perpendicular to the waveguide layers (*x* direction in Fig. 1), SPs propagate preferentially in the vertical direction. To achieve a broad spreading of SPs in the lateral direction, the size of the aperture has to be optimized. If the dimensions of the aperture are much smaller than the laser wavelength λ, the aperture functions effectively as a point source of SPs when illuminated by the laser beam. In this case the amplitude of the SPs follows a $\cos\theta$ dependence, where θ is the angle from the laser polarization direction [27-29]; see Fig. 1. The intensity of the SPs then follows a $(\cos\theta)^2$ rule. Therefore, one gets substantial SP diffraction at large θs: for instance, at θ=45^o, the intensity of the SPs is 50% of the maximum. However, the drawback of a small aperture is that it strongly limits the power emerging from the laser cavity. A larger aperture increases the mirror loss, increasing accordingly the slope efficiency of the lasers. This enables the devices to achieve higher maximum optical power. As one increases the aperture size to couple more power out, the point-source approximation is not valid any more and the divergence of the SPs, governed by diffraction, progressively decreases. This process would result in a less efficient collimation in the lateral direction. In the real case, a trade-off is thus to be sought between power outflow and collimation.

We simulated a passive structure (no gain for the laser active region) consisting of a small section (~10 μm) of the laser waveguide adjacent to the laser facet. In our simulations, we solved a stationary problem by applying an incident field to the backend of the laser waveguide. The transmitted power was calculated by integrating the power outflow on a hemisphere outside the device enclosing the aperture and the grating. We used complex optical constants for different materials and appropriate boundary conditions for the simulation region.

We performed systematic simulations to study the evolution of the power outflow and the SP divergence as a function of the lateral aperture size w_1. We assume that the lasers emit at λ=8.06 μm, which matches the wavelength of our BHT laser samples. The optical mode inside the laser waveguide is the fundamental TM_{00} mode with an elliptical mode profile overlapping with the active core, which has a cross section of 2.1 μm×9.7 μm in the vertical and lateral directions. The vertical aperture size w_2 is chosen to approximately equal the thickness of the laser active core: smaller w_2 would limit the power throughput while larger w_2 would result in reduced efficiency of coupling into SPs and increased optical background in the far field.

Figure 2(a) is a typical 2D simulation result showing the intensity ($|E|^2$) of the SPs for a λ=8.06 μm device patterned with a $w_1 \times w_2$=4×2 μm^2 aperture and 20 grooves. The SPs are seen to spread widely in a 2D way on the laser facet. In Fig. 2(b) and (c), the simulation results for devices with different w_1 patterned with 10 and 20 rings are summarized. Figure 2(b) shows that small apertures (2×2 μm^2) give a FWHM SP intensity divergence angle very close to 90^o consistent with the prediction of the $(\cos\theta)^2$ rule. Significant lateral propagation of SPs is still observed when w_1 is nearly equal to the free-space wavelength 8.06 μm (Fig. 2(b)) while the power output is greatly improved (a factor of 10 compared to an aperture with w_1=4 μm; see Fig. 2(c)). We performed near-field to far-field transformation algorithm [30] to determine the beam divergence in the far field based on the calculated near-field distributions. Figure 2(d) summarizes the calculated far-field divergence angles in the vertical and lateral

#100120 - $15.00 USD Received 13 Aug 2008; revised 19 Sep 2008; accepted 21 Sep 2008; published 10 Nov 2008

directions for the devices with 10 and 20 rings. The slight difference between the two sets of data for 20 and 10 rings presented in Fig. 2(b) is most probably due to the fact that we are monitoring the SP divergence at different distances away from the aperture. The SP divergence angle is calculated on the 9^{th} groove in the device with 10 rings and on the 13^{th} groove in the device with 20 rings. The difference in power transmission in Fig. 2(c) is likely due to the loss in the metal: the device with 20 rings have much larger simulation area and accordingly larger loss.

2.3 Grating period

The half-ring grating in our design is intended to scatter SPs into free-space propagation normal to the facet. The period of the grating was thus chosen to match the wavelength of the SPs on the patterned metal surface (second-order grating [21,22]). Introducing a grating modifies the SP dispersion curve: optical band gaps are opened, just as energy band gaps appear when an electron experiences the periodic potential of an ordered crystal lattice [31]. We cannot use the theoretical value of the SP wavelength on a *flat* interface to design the grating, because such a grating corresponds to a point in the band gap and therefore prohibits the propagation of SPs. We conducted simulations to adjust the grating period to be equal to the wavelength corresponding to the upper edge of the bandgap. The optimized grating period is found to be 7.8 μm for λ=8.06 μm.

2.4 Position of the grating relative to the aperture

The position of the grating structure relative to the aperture, i.e. the radius of the first ring r_1 was tuned to achieve maximum constructive interference between the beam directly emerging from the aperture and the ones scattered by the grooves. Choosing r_1 equal to the grating period is usually not optimal owing to the complex form of the field in the near zone around a metallic aperture. Complete understanding of this near field has not yet been achieved [32-34], but these work finds that it contains both SPs with wavevector k_{sp} and another type of lossy surface waves with a wavevector larger than k_{sp}, which is damped much faster than SPs. Effectively, this near field exhibits a gradual increase of wavelength: its wavelength is smaller closer to the aperture and progressively approaches the SP wavelength as the distance from the aperture increases. Accordingly, we selected an r_1 that is smaller than the grating period to ensure the constructive interference condition mentioned above. We performed simulations to help determine the optimal r_1.

2.4 Width, depth, and number of grooves

The number of grooves N is critical for the collimator; it is favorable to have as many grooves as possible to reduce the divergence angle and to increase the collimated power. However, adding grooves will only have an impact if the SPs can reach them. The propagation distance of SPs is thus the intrinsic limit. Heat generation in the metal and scattering by the surface roughness are two main sources of energy losses. Taking these into consideration, SPs can propagate over a few millimeters at mid-ir wavelengths [35]. In our particular structure, the desired scattering into free space by the grating grooves acts as an additional factor limiting the propagation distance. The grating should be designed to provide a uniform scattering along the propagation of SPs.

Two possible designs were considered for the grooves, either shallow and wide ones or deep and narrow ones. In the first case, undesired back reflections of SPs can be suppressed

#100120 - $15.00 USD Received 13 Aug 2008; revised 19 Sep 2008; accepted 21 Sep 2008; published 10 Nov 2008

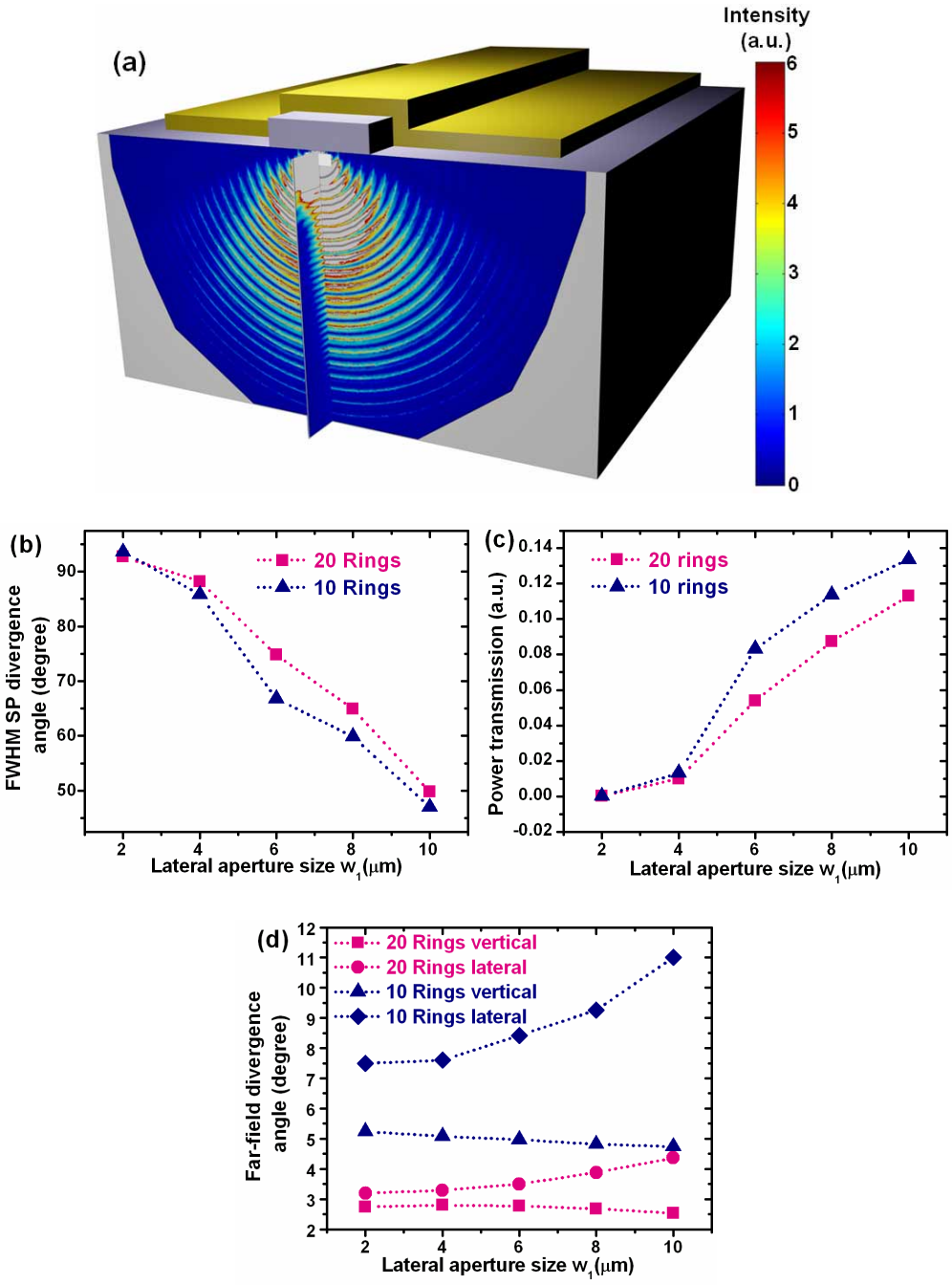

Fig. 2. (a) Simulated near-field intensity of the SPs. The SPs are highly localized on the device facet: their half-intensity decay length is approximately 3 μm away from the facet. Two cross sections of the intensity are represented: one parallel to the laser facet, at 100 nm above the facet, the other perpendicular to the laser facet, along the axis of symmetry of the half-ring pattern. (b) Simulated FWHM dispersion angles of SPs as a function of the lateral aperture size w_1. (c) Power transmission as a function of w_1 for devices with 10 and 20 rings. Power transmission is defined as all the transmitted power (including the far-field component and the near field one that is not scattered into the far field by the grating) divided by the power launched into the laser waveguide. (d) Simulated far-field divergence angles in the vertical and lateral directions for the devices with 10 and 20 rings. In all the simulations the vertical aperture size w_2 is kept constant at 2 μm.

#100120 - $15.00 USD Received 13 Aug 2008; revised 19 Sep 2008; accepted 21 Sep 2008; published 10 Nov 2008

with a symmetric grating (duty cycle 50%) [36]. the reflection of SPs is weak and the scattering efficiency is mainly controlled by the groove width *w* and depth *d*. Indeed, a resonant behavior of the field scattered by the grooves with respect to their depth *d* is reported in Ref. [32]. The resonance can be understood as resulting from the creation of standing waves along the depth of the narrow grooves, i.e. groove cavity modes [23,32]. The resonance condition is essential for achieving the optimal collimation effect [23]. However, the groove cavity resonance modifies the phase of the scattered light from the grooves [23,32], so that the groove depth *d*, the grating period Λ, and the radius of the first groove r_1 should be adjusted together to make sure that the direct emission from the aperture and the sub-emissions from the grooves are in phase.

Based on simulations of different designs, we chose the design with narrow and deep grooves and adjusted the groove width and depth to 0.6 μm and 1 μm, respectively, to give the best collimation results. Our simulations show that mid-ir SPs are able to propagate at least a few hundred microns in the presence of grating grooves, which enables one to use up to tens of rings. A list of the optimized design parameters is summarized in Table 1.

Table 1. Optimized design parameters for λ=8.06 μm and λ=9.95 μm QCLs

	grating period Λ (μm)	groove width *w* (μm)	groove depth *d* (μm)	radius of the first groove r_1 (μm)
λ=8.06 μm BHT QCLs	7.8	0.6	1.0	6.0
λ=9.95 μm ridge QCLs	9.4	0.8	1.5	7.2

3. Fabrication and measurement

We fabricated 2D plasmonic collimators on both ridge QCLs and BHT QCLs. The ridge devices lase at $\lambda \approx 9.95$ μm and are grown by molecular beam epitaxy; the BHT devices lase at $\lambda \approx 8.06$ μm and are grown by metal organic vapor-phase epitaxy [37]. The ridge devices have 2.1-μm active-region thickness and various active-region widths. The active region of all the BHT devices used has a cross section of 2.1 μm×9.7 μm in the vertical and lateral directions.

The fabrication procedure starts with focused ion beam (FIB) milling of half-ring grooves in the indium phosphide (InP) substrate of QCLs. Next, a 200-nm-thick alumina film is deposited onto the laser facet for electrical insulation using electron-beam evaporation, and a 600-nm-thick gold film is deposited using thermal evaporation. Multi-angle deposition is implemented such that the walls of the grooves are also covered by the alumina and gold film. Finally, FIB milling is used a second time to open the aperture through the gold film in front of the laser active core. We chose a procedure in which grooves are cut into semiconductors before any deposition instead of one in which a thick gold film is deposited first and the grooves are cut into it afterwards [21,22]. Because FIB mills smooth features in a semiconductor while milling in a metal usually results in pronounced roughness due to large size of the crystallites in the metal.

To map the 2D far-field emission patterns of the devices, we used a set-up consisting of two motorized rotation stages. The tested devices were mounted on one of the rotation stages and could be rotated in the vertical plane. A mid-ir mercury-cadmium-telluride detector was mounted on the other stage and could be scanned across a certain angle in the horizontal plane. The distance between the devices and the detector was kept constant at about 15 cm. Our measurements were performed with a resolution of 0.25^o. Power measurements were carried out with a calibrated power meter. The power meter, which has a metallic collection tube with a diameter of 6.5 mm, was placed within 2 mm of the lasers, thus collecting emitted power in an angular range of approximately $\pm 60^o$ with respect to the normal of the laser facet. A Fourier-transform infrared spectrometer was used for spectral measurements.

#100120 - $15.00 USD Received 13 Aug 2008; revised 19 Sep 2008; accepted 21 Sep 2008; published 10 Nov 2008

4. Experimental results

A thorough study was performed for λ=8.06 μm BHT QCLs patterned with plasmonic collimators. The original devices with unpatterned facets have divergence angles of $\theta_{||}$=42°, $\theta_{\perp}$=74° (Fig. 3). Figure 4(a) and (c) show two representative devices patterned with (a) 10 and (c) 20 grooves and with small aperture size (a) $w_1 \times w_2$=2.8×1.9 μm^2 and (c) 2.1×1.9 μm^2. The far-field intensity profiles are shown in Fig. 4(b) and (d) for the two devices, respectively. Compared to the unpatterned devices, the ones patterned with the 2D collimators exhibit greatly reduced divergence angle: $\theta_{||}$ and $\theta_{\perp}$ equal to 8.6° and 5.1°, respectively, for the device with 10 rings and equals to 3.7° and 2.7°, respectively, for the one with 20 rings. It is evident from Fig. 4(b) and (d) that the device with 10 rings has a larger optical background outside of the central beam compared with the device with 20 rings. As a useful figure of merit we borrow the concept of antenna directivity for device characterization, taking into account both beam divergence and optical background. The directivity is defined as $D=10log_{10}(2\pi I_{peak}/I_{total})$, where I_{peak} is the far-field peak intensity, and I_{total} is the total intensity under the 2D far-field beam profile. While D is only about 8.3 dB for the unpatterned lasers, we calculated based on our experimental results that it is 17.3 and 26.9 dB for the devices with 10 and 20 rings, respectively. The performance improvement with the number of rings is consistent with our simulations.

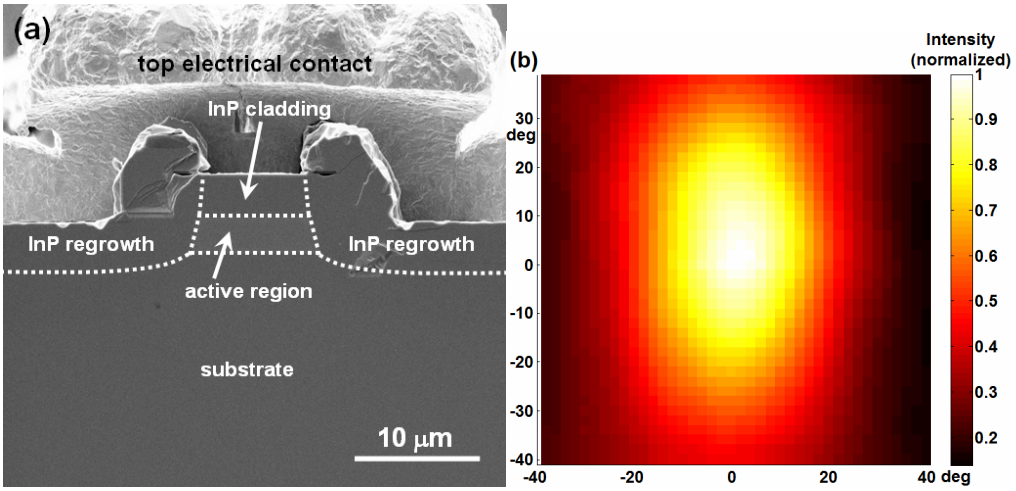

Fig. 3. (a) An electron micrograph showing the facet of an unpatterned λ=8.06 μm BHT QCL. (b) The 2D far-field intensity profile of the device.

#100120 - $15.00 USD Received 13 Aug 2008; revised 19 Sep 2008; accepted 21 Sep 2008; published 10 Nov 2008

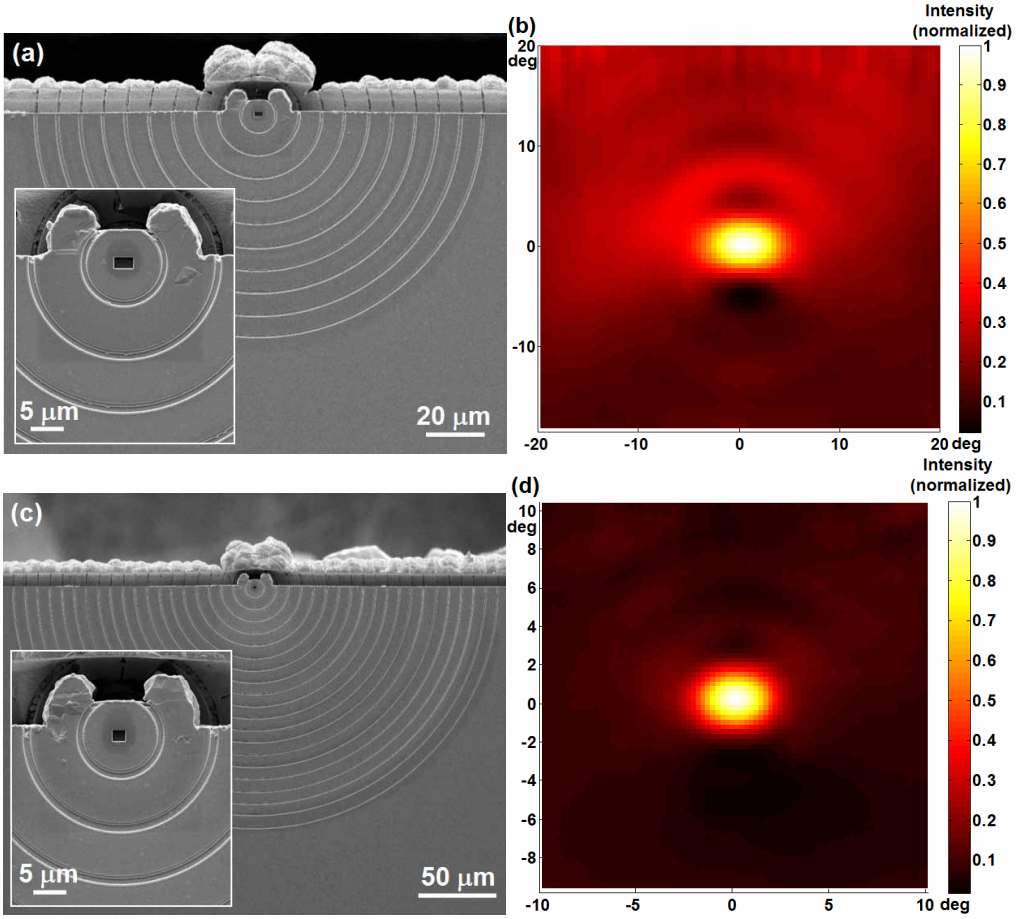

Fig. 4. Far-field measurement results of two λ=8.06 μm BHT QCLs with small apertures. (a) and (c) Electron micrographs of the two devices patterned with 10 and 20 grooves, respectively. Insets are zoom-in views. The two devices have aperture size $w_1 \times w_2$=2.8×1.9 and 2.1×1.9 μm^2, respectively. (b) and (d) Measured 2D far-field intensity profiles for the two device, respectively. The far-field measurements were performed while the lasers were operated in pulsed mode with 80-kHz repetition rate and 1% duty cycle.

Central to our design considerations discussed above is the lasing wavelength. This quantity determines the SP wavelength and therefore the optimal grating period. Other parameters of the design such as the radius of the first ring groove r_1 and the groove width w and depth d are also optimized only for this particular wavelength. However, the BHT devices used have multiple longitudinal modes: the central wavelength is at λ=8.06 μm and the spectrum width $\Delta\lambda$ usually broadens at a large driving current I_{dr}; see Fig. 5. For instance, $\Delta\lambda$ is approximately 0.1 μm at I_{dr}=500 mA; it quickly increases to about 0.3 μm at I_{dr}=600 mA and stays around 0.3 μm at larger I_{dr} up to 1.0 A. It is thus expected to give larger laser divergence at a higher driving current. However, we found that the far-field divergence angle measured was relatively stable at different driving currents. For instance, for the device with 10 rings, $\theta_\perp$ equals to 5.0, 5.1 and 5.1 degrees, while $\theta_{||}$ equals to 8.5, 8.6, and 8.6 degrees at I_{dr}=500, 600, and 800 mA, respectively; for the device with 20 rings, $\theta_\perp$ equals to 2.6 and 2.7 degrees, while $\theta_{||}$ stays at 3.7 degrees at I_{dr}=500 and 600 mA, respectively. The directivities at these currents were found to be nearly constant for the two devices. These observations demonstrated that the ring collimator design is robust with respect to laser spectral broadening. To understand

#100120 - $15.00 USD Received 13 Aug 2008; revised 19 Sep 2008; accepted 21 Sep 2008; published 10 Nov 2008

this phenomenon we conducted simulations and analytical calculations to investigate the effect of spectrum broadening on the beam divergence. Simulations show that a shift of lasing wavelength by 0.1 μm causes a shift of the far-field direction angle by approximately 1°. This appears large but one should consider that the peaks, i.e. longitudinal modes, in the spectra are very dense and centered around λ=8.06 μm and that the modes farther from the center wavelength have smaller intensity; see Fig. 5. Analytical calculations indicate that there is just a ~0.3° increase of the FWHM far-field divergence angles when one considers the contributions of all the modes in the broad spectra.

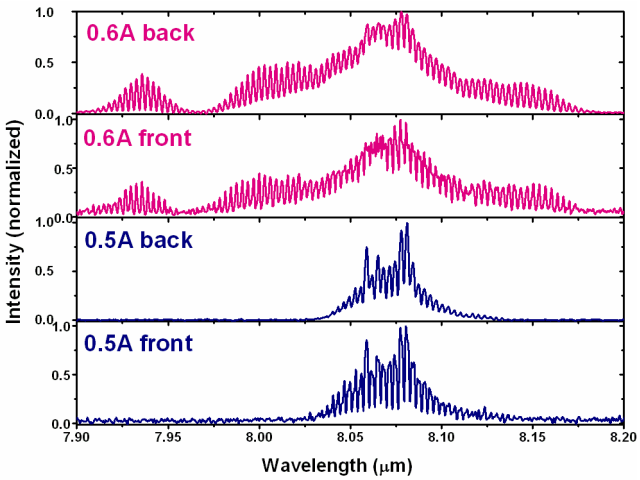

Fig. 5. Spectra of the device patterned with 20 rings. Top two panels and lower two panels were taken at I_{dr}=600 and 500 mA, respectively. Spectra taken from both the front facet (patterned with the collimator) and the back facet (uncoated) are quite similar.

We stepwise increased the aperture width w_1 of the above devices using FIB milling to investigate the impact of this parameter on $\theta_\perp$, $\theta_{||}$ and the power output. We kept the vertical aperture size w_2=1.9 μm. The light output versus current (LI) characteristics of the devices for different aperture sizes are shown in Fig. 6. Figure 7 summarizes the measured far-field beam divergence angles for different aperture sizes; plotted are also calculated far-field beam divergence angles. The slope efficiency for the devices increases as expected with increasing aperture width (Fig. 6), leading to a higher maximum power. At the same time the lateral divergence angle $\theta_{||}$ increases, while $\theta_\perp$ is nearly a constant (Fig. 7). The behavior of $\theta_{||}$ is due to the narrowing of the SP divergence angle on the laser facet as presented in Fig. 2(b); see Fig. 8 for the far-field intensity profiles of the devices with wide apertures. For the widest apertures investigated in this work (10.1 μm for the device with 10 rings and 8.1 μm for the one with 20 rings) the maximum output power P_{max} was more than 50% of that of the original unpatterned laser, while the divergence angles are still significantly reduced compared to the original unpatterned device. For instance, 53% of the original P_{max} was measured for the device with 20 grooves (Fig. 6(b)) with a divergence of only $\theta_\perp$=2.4° and $\theta_{||}$=4.6° (Fig. 8(d)). The dependence of the maximum power and the divergence angles on the aperture width w_1 are summarized in Table 2.

#100120 - $15.00 USD Received 13 Aug 2008; revised 19 Sep 2008; accepted 21 Sep 2008; published 10 Nov 2008

Table 2. Divergence angles and power output as a function of lateral aperture size w_1

Device with 10 rings			Device with 20 rings		
Aperture size $w_1 \times w_2$ (μm^2)	FWHM far-field divergence angles $\theta_\perp$, $\theta_{\|\|}$ (degrees)	Maximum power compared to the original laser	Aperture size $w_1 \times w_2$ (μm^2)	FWHM far-field divergence angles $\theta_\perp$, $\theta_{\|\|}$ (degrees)	Maximum power compared to the original laser
2.1×1.9	5.1, 8.6	18%	2.8×1.9	2.7, 3.7	11%
5.0×1.9	5.1, 9.2	33%	5.0×1.9	2.7, 3.7	37%
7.5×1.9	5.2, 10.1	45%	8.1×1.9	2.4, 4.6	53%
10.1×1.9	4.5, 11.4	56%			

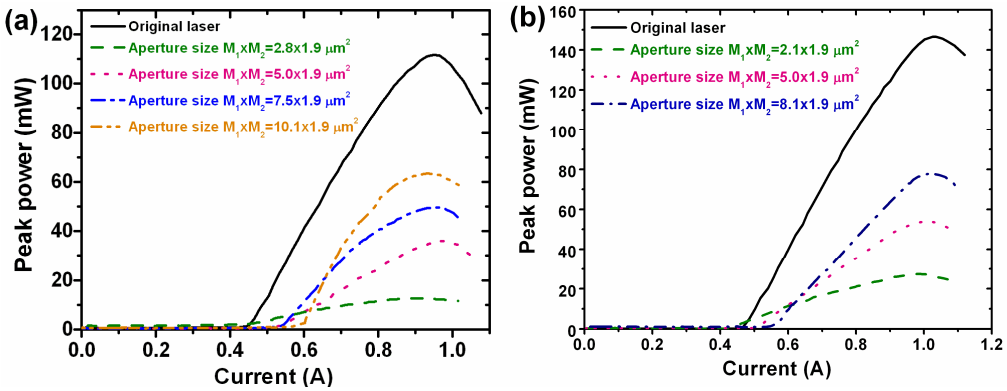

Fig. 6. LI characteristics for the two BHT devices. (a) and (b) are for devices patterned with 10 and 20 rings, respectively. Shown are LI curves taken both for the original unpatterned devices and the ones with different aperture size. In all the measurements, the lasers are operated at room temperature in pulsed mode with 80-kHz repetition rate and 1% duty cycle.

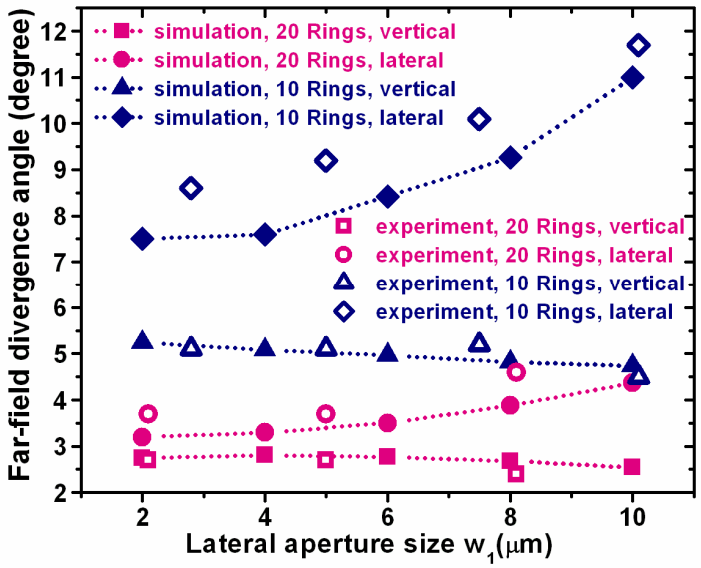

Fig. 7. Divergence angles in the vertical and lateral directions as a function of the lateral aperture size w_1. Calculation results are represented with filled symbols and experimental results are represented with hollow symbols.

#100120 - $15.00 USD Received 13 Aug 2008; revised 19 Sep 2008; accepted 21 Sep 2008; published 10 Nov 2008

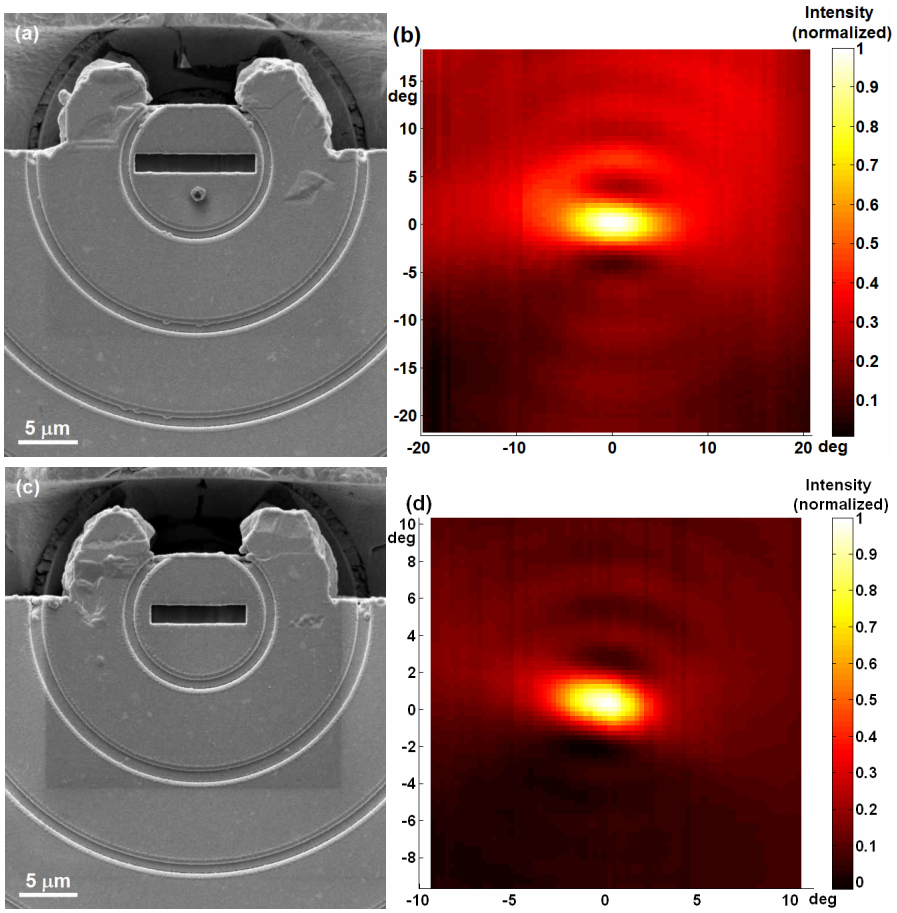

Fig. 8. Characterizations of the two BHT QCLs with large apertures. (a) and (c) Electron micrographs showing the zoom-in views of the facets of the two devices patterned with 10 and 20 grooves, respectively. The two devices have aperture size $w_1 \times w_2$=10.1×1.9 and 8.1×1.9 μm^2, respectively. (b) and (d) Measured 2D far-field intensity profiles for the two device, respectively.

The LI curves also illustrate the dependence of the lasing threshold with w_1 (Fig. 6). A small aperture corresponds to the laser active core being mostly covered by gold. The effective reflectivity R_{eff} of the facet is thus increased and, as expected, the threshold is reduced in comparison to the original devices. As w_1 is increasing, the device experiences a gradual increase of the lasing threshold. The devices exhibit a larger threshold compared with the original devices when w_1 is comparable to the active region width. This is most probably due to the complex scattering and coupling to SPs at the aperture, which leads to a reduced R_{eff}.

Figure 7 shows that there is reasonably good agreement between the calculated and the measured vertical far-field divergence angles, but the measured lateral divergence angles are constantly larger than the calculated values by about 20%. This is probably due to the fact that we did not take into consideration the detailed geometry of the InP regrown regions of the BHT lasers (Fig. 3(a)) and simply modeled the laser waveguide as rectangular (Fig. 1). The two humps at the edges of the laser ridge, that are formed during regrowth of the ridges for BHT processing, are adjacent to the first ring groove (for instance, see Fig. 8(c)) and may scatter the SPs in an unpredictable manner, affecting their lateral spreading and eventually the

#100120 - $15.00 USD Received 13 Aug 2008; revised 19 Sep 2008; accepted 21 Sep 2008; published 10 Nov 2008

lateral far-field divergence. Since the SPs are preferentially generated in the vertical direction, the SPs propagating in this direction are less affected and therefore the measured and calculated vertical divergence match well each other.

As discussed above, the spreading of the SPs on the facet is essential to achieve lateral collimation. The structure presented in Fig. 9 (the so-called "spider's web" structure) may give us some insight into the SP divergence. Fig. 9(b) demonstrates that the far field pattern of this device is a superposition of several stripes: the stripes numbered from 1 to 4 in Fig. 9(b) correspond to, respectively, the gratings in Fig. 9(a), labeled from 1 to 4. This far-field pattern indicates that SPs spread widely on the laser facet: they are mainly distributed within $\pm 45^{o}$ with respect to the laser polarization direction, but outside this angle range, there is still substantial SP diffraction. The ratio between the intensity of the intense stripes and that of the weak ones in Fig. 9(b) may serve as a rough estimation of the angular distribution of SPs.

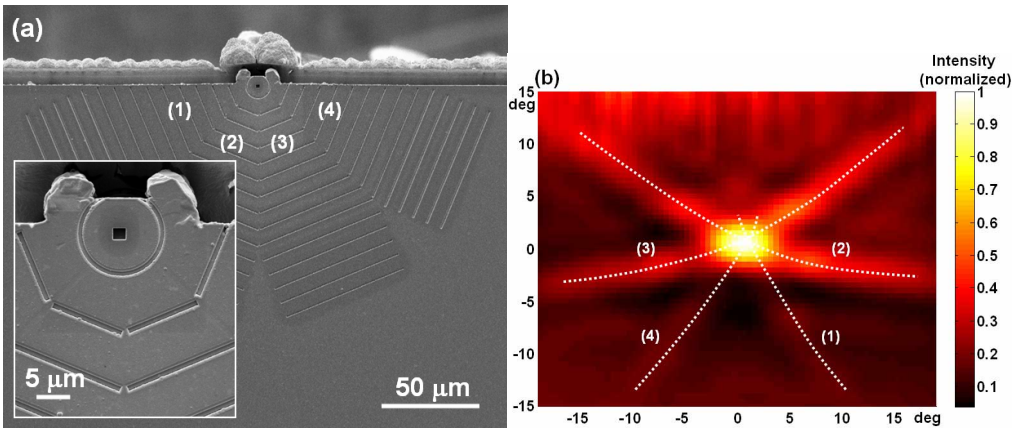

Fig. 9. Experimental results for the "spider's web" design. (a) Electron micrograph of a device facet with a "spider's web" pattern consisting of an aperture and four gratings. Inset is zoom-in view. (b) Measured far-field intensity profile for the device. Different stripes, numbered from 1 to 4 in Fig. 8(b), can be distinguished, corresponding to, respectively, the gratings in Fig. 8(a), labeled from (1) to (4).

Ridge waveguide QCLs can be easily processed compared with the BHT QCLs, which need regrowth of semi-insulating side cladding layers. It is therefore instructive to show that the 2D plasmonic collimator design also works for devices with ridge waveguides. Although ridge QCLs have less facet area for patterning compared with the BHT devices, we successfully demonstrated ring collimators on λ=9.95 μm ridge QCLs. A simple scaling of the optimized design parameters for the λ=8.06 μm BHT devices was found to give essentially the right parameters for the ridge devices. A list of the optimized design parameters is summarized in Table 1. An electron micrograph of a representative ridge device with ring collimator and its far-field emission profile are presented in Fig. 10(a) and (b), respectively. The experimental performance of this device is comparable to the one obtained with BHT devices with the same number of grooves: its divergence angles are $\theta_{\perp}$=5.0^{o} and $\theta_{||}$=8.1^{o}, while its directivity D is about 16.2 dB.

#100120 - $15.00 USD Received 13 Aug 2008; revised 19 Sep 2008; accepted 21 Sep 2008; published 10 Nov 2008

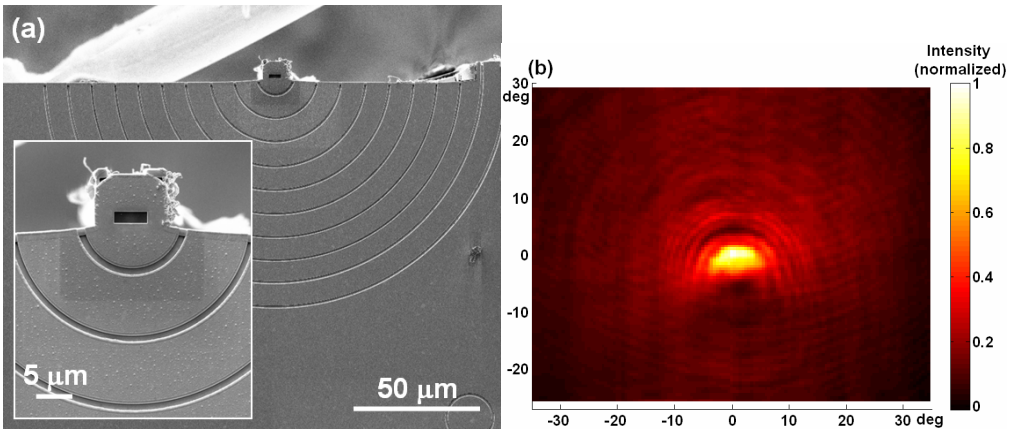

Fig. 10. Experimental results for a λ=9.95 μm ridge QCL. (a) An electron micrograph showing the device facet. Inset is a zoom-in view. (b) Measured far-field intensity profile for the device. The far-field measurements were performed while the lasers were operated in pulsed mode with 80-kHz repetition rate and 1% duty cycle.

5. Conclusion

In conclusion, we have performed systematic experiments and simulations to demonstrate that the integration of a suitably designed 2D aperture-grating structure on the facet of QCLs reduces the beam divergence angles by a factor up to ~30 and ~10 in the vertical and lateral directions, respectively, down to 2.7^o and 3.7^o. The optimized devices preserve a high output power, comparable to that of the unpatterned lasers. We have shown that the 2D plasmonic collimator design is applicable to both BHT and ridge devices. We plan to investigate optimized aperture shapes to enhance the output power and extend the concept of plasmonic collimation to visible or near-infrared edge-emitting laser diodes and VCSELs. More generally, it would be important for applications to design and build plasmonic nanostructures or even metamaterials on the facet of any type of semiconductor lasers and also on fiber lasers to achieve complex wavefront engineering, such as novel beam shaping and polarization control. The technique used to fabricate plasmonic collimators based on FIB milling has the problem of high cost and low throughput. We plan to use soft-lithographic techniques such as imprint lithography [38] and microcontact printing [39] for patterning plasmonic structures. These methods would allow low-cost parallel procession.

Acknowledgments

We acknowledge support from the Air Force Office of Scientific Research (AFOSR MURI on Plasmonics) and the Harvard Nanoscale Science and Engineering Center (NSEC). This work was performed in part at the Center for Nanoscale Systems (CNS) at Harvard University, a member of the National Nanotechnology Infrastructure Network (NNIN), which is supported by the National Science Foundation under NSF award no. ECS-0335765. CNS is part of the Faculty of Arts and Sciences at Harvard University.

#100120 - $15.00 USD Received 13 Aug 2008; revised 19 Sep 2008; accepted 21 Sep 2008; published 10 Nov 2008